Small-Signal-Stability Enhancement using a Power-System Stabilizer based on the Cuckoo-Search Algorithm against Contingency N-1 in the Sulselrabar 150-kV System

by Awan Uji Krismanto

Stability of Renewable Energy based Microgrid in Autonomous Operation

Awan Uji Krismanto, N. Mithulananthan *, Olav Krause

University of Queensland, Brisbane, Australia

ARTICLE INFO

ABSTRACT

This paper develops a comprehensive small-signal model of hybrid renewable-energy-based microgrid (MG) in an attempt to perceive oscillatory stability performance and capture the potential interaction between low-frequency critical modes within the MG. Trajectories of sensitive modes due to controller gain variations were evaluated in order to determine the stability boundaries. It was noticeable that various power-sharing schemes significantly influenced the small-signal stability of MG. Moreover, modal interaction emerged due to the proximity of RES-based DG units and non-linear dynamic behaviour of the sensitive modes. The interaction may result in a more oscillatory situation which potentially leads to instability of MG. The low-frequency critical modes obtained from eigenvalues analysis were then verified with the help of nonlinear time domain simulations. The presented work contributes to enhance the design and tuning of controller gain and propose appropriate power-sharing scheme within MG.

© 2017 Elsevier Ltd. All rights reserved.

1. Introduction

The penetration of renewable energy resources (RES) based distributed generation (DG) has been increasing intensively in recent years due to their beneficial impacts in bringing clean energy and lowering the dependency on fossil fuel. Among various RES, photovoltaic (PV) and wind energy conversion system (WECS) have been considered as the most deployed DG units due to their favourable technical and economic benefits [1,2]. On the other hand, the major concern in developing stand-alone PV or WECS based power generations is how to maintain the continuity of electricity supply. These concerns not only influence reliability of electricity supply but also require over-sizing of energy storage system (ESS) to manage with frequent early discharge due to RES fluctuations [3]. According to the limitations of individual DG unit, it is necessary to organize a cluster of DG units into a single controlled and coordinated power system known as Microgrid (MG).

Similar to conventional power system, the stability issues in MG can be classified into transient, voltage and small signal stability. Transient stability concern in MG corresponded to the ability of MG to maintain a stable condition after being subjected to large disturbances such as short-circuit faults, structural change in MG due to the outage of a particular DG unit and operation mode switching from grid connected to islanding operation [4]. Transient instability problem is not a big concern in MG as the generating

units considered are relatively small and mostly not synchronous machine based. MG should be able to maintain acceptable *voltages* at all buses under normal condition and after being exposed to a disturbance. Voltage stability problem in MG mostly emerges due to the connection of dynamic loads, reactive power limit and tap changer operation [5]. Moreover, the MG is susceptible to the occurrence of small perturbations as a consequence of having a cluster of RES based DG units with less physical inertia. Lack of system damping condition in a MG might lead to the undamped oscillatory condition when it is subjected to small disturbances such as fluctuating RES condition, small load change and parameter variations [5–9]. Therefore, a comprehensive study of small-signal stability in MG is crucial to ensure stable operation of MG.

A limited amount of small-signal stability analysis considering different RES based DE units in MG was presented in the literature so far. In [10,11], the small-signal stability analysis of wind-based MG was provided. However, the presented analysis neglected WECS dynamic behaviour and control system. In previous small-signal stability studies, power electronic devices in DG units are usually presented as an ideal voltage source which may lead to inaccurate results [12–14]. Practically, various architectures of power electronic devices are employed to get the most advantages from the RES. Therefore, different dynamic responses of DG units might emerge when various RES-based power generations are integrated into a MG. Those typical dynamic behaviours cannot be captured by using the simplified model as developed in the previous literature. A comprehensive MG model considering all possible dynamics from each of the DG units is required to provide a complete picture of small-signal stability of MG. Moreover, in

* Corresponding author.
E-mail addresses: a.krismanto@uq.edu.au (A.U. Krismanto),
mithulan@itee.uq.edu.au (N. Mithulananthan), o.krause@uq.edu.au (O. Krause).

Nomenclatures

Line and Load

i_{likDQ}	D and Q axis line current.
i_{loDQ}	D and Q axis load current.
v_{bkDQ}	D and Q axis local bus voltage.

Bio-Diesel (BDG) Generator

i_{kq1}, i_{kq2}	q axis rotor current.
i_{kd}	d axis rotor current.
i_{sdq}	d and q axis stator current.
i_{fd}	d axis field winding current.
T_{Mde}	Mechanical torque.
v_{fd}	d axis field winding voltage.
v_{sdq}	d and q axis stator voltage.
ω_{ref}	Angular frequency.
δ_d	Phase angle.

Two-stages PV system

i_b	DC/DC converter input current.
i_s	DC/DC converter output current.
v_b	DC/DC converter output voltage.
v_{dc}	DC link/DC side voltage of DC/AC inverter.
ρ_{pv}	Auxiliary control state variable of DC/DC converter
δ_{pv}	Phase angle of PV system.
p_{pv}	Active power of PV system.
q_{pv}	Reactive power of PV system.
φ_{pvdq}	PV voltage control loop state variables.
β_{pvdq}	PV current control loop state variables.
i_{idq}	d and q axis DC/AC inverter current.
v_{odq}	d and q axis output voltage.
i_{odq}	d and q axis output current.
i_{opvDQ}	D and Q axis PV output current in common reference frame.
v_g	Input voltage of PV system.
n_p	PV active power droop gain.
n_q	PV reactive power droop gain.

Wind Energy Conversion System (WECS) Induction generator

i_{sdq}	d and q axis stator current.
i_{rdq}	d and q axis rotor current.
ω_w	Angular frequency.
v_{sdq}	d and q axis stator voltage.
v_{sdq}	d and q axis stator voltage.
v_{rdq}	d and q axis rotor voltage.

DC/AC/DC system

γ	State variable of reference current calculation in Flux Oriented Control (FOC).
ρ_{wdq}	FOC state variables.
i_{indq}	d and q AC/DC converter current.
v_{dqin}	d and q input voltage of AC/DC converter.
δ_w	Phase angle of WECS.
p_w	Active power of WECS.
q_w	Reactive power of WECS.
φ_{wdq}	WECS voltage control loop state variables.
β_{wdq}	WECS current control loop state variables.
i_{iwdq}	d and q axis DC/AC inverter current.
v_{owdq}	d and q axis output voltage.
i_{owdq}	d and q axis output current.
v_{sdq}	d and q axis stator voltage.
v_{rdq}	d and q axis rotor voltage.
T_w	Mechanical torque.

a MG with a cluster of DG units, the interaction among sensitive eigenvalues potentially exhibit. Investigation of modal interaction is needed since the occurrence of interaction introduces more oscillatory conditions and deterioration of stability performance.

Detailed MG model was primarily developed in [15]. However, the control systems were not considered in the research. Hence, this paper develops a detailed model of each DG unit in MG to provide a comprehensive study and better understanding of MG small-signal stability performance under autonomous operation. A hybrid MG consists of WECS, PV and Bio-Diesel (BDG) generator is considered in this work. Trajectories of the low-frequency critical modes on different power sharing strategies and gain control variations are mapped to determine the small-signal stability boundaries. Moreover, the possibility of modal interaction between nearby eigenvalues is thoroughly analysed. Time-domain simulation is then performed to verify and visualize the trajectories of eigenvalues analysis.

Rest of the paper is organized as follows. A step-by-step comprehensive modelling of PV-Wind-Diesel MG for small-signal investigation and a general summary of MG modelling is presented in Section 2, along with a brief methodology of small-signal stability and modal interaction. Section 3 describes the simulation results in details. Conclusions and contributions of this paper are highlighted in Section 4.

2. State–space model of hybrid microgrid

Fig. 1 represents a typical model of MG system in a generic distribution network. Under islanding mode, a synchronized operation is mandatory to maintain a stable MG operation. Therefore, it is necessary to translate all individual reference frame (dq) of each DG unit into a common reference frame (DQ) which is provided by a reference DG unit. The reference DG can be performed by a synchronous machine based DG such as bio diesel generator (BDG) or an inverter based DG equipped with the controller to establish a given voltage magnitude and frequency [16]. Translation from the individual to the common reference frame is facilitated using transformation matrices of $\mathbf{T_{c\delta}}$ and $\mathbf{T_f}$. While, reverse transformation is conducted using inverse transformation matrices of $\mathbf{T_{v\delta}}$ and $\mathbf{T_f^{-1}}$ [17].

Bus voltages are considered as input variables that provide a connection to each subsystem. The bus voltages $\left(\Delta v_{kDQ}\right)$ can be accurately estimated using the following equation [17]

$$\Delta v_{kDQ} = R_N \left(\Delta i_{oDQ}\right) - R_N \left(\Delta i_{loDQ}\right) + R_N \left\{\left(\Delta i_{likDQ}\right)_{in} - \left(\Delta i_{likDQ}\right)_{out}\right\} \tag{1}$$

where R_N is virtual resistance, Δi_{oDQ} represents the output current of DG unit connected to the bus k. Δi_{loDQ} is related to the load current at bus k. While the $\left(\Delta i_{likDQ}\right)_{in}$ and $\left(\Delta i_{likDQ}\right)_{out}$ corresponding to a given line current entering and leaving the kth bus, respectively.

In the following sections, modelling procedure of line impedances, load, and the DG units are presented. A comprehensive state–space model of BDG, two-stages PV and fully-rated WECS based DG units are developed to examine a complete small-signal stability performance of islanding MG operation.

2.1. State-space model of line impedances

Distribution lines presented in Fig. 1 are modelled as series RL elements. The linearized state–space equations of line impedance between m and n nodes is given in (2) a generalized form.

$$\Delta \dot{\mathbf{x}}_{\mathbf{line}} = \mathbf{A_{line}} \Delta \mathbf{x_{line}} + \mathbf{B_{line1}} \Delta \mathbf{v_{mDQ}} + \mathbf{B_{line2}} \Delta \mathbf{v_{nDQ}} + \mathbf{B_{\omega li}} \Delta \omega_{ref} \tag{2}$$
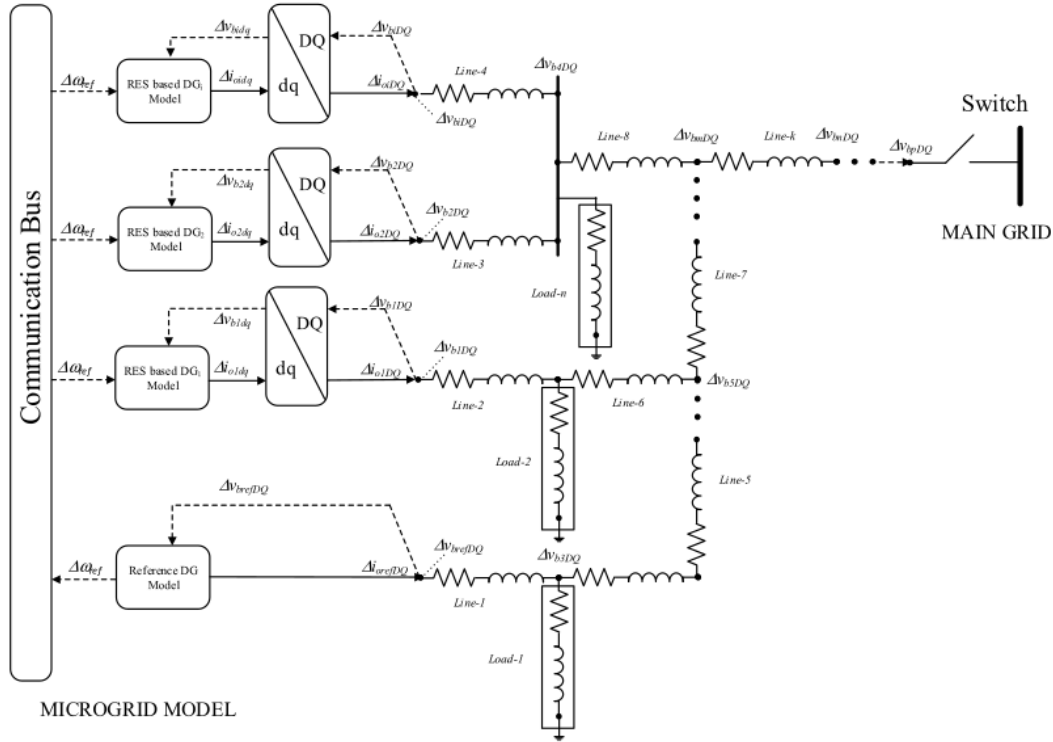
Fig. 1. Typical MG structure in a distribution network.

where $\boldsymbol{\Delta x_{line}} = \begin{bmatrix} \Delta i_{likD} & \Delta i_{likQ} \end{bmatrix}^T$, $\boldsymbol{\Delta v_{mDQ}} = \begin{bmatrix} \Delta v_{mD} & \Delta v_{mQ} \end{bmatrix}^T$, $\boldsymbol{\Delta v_{nDQ}} = \begin{bmatrix} \Delta v_{nD} & \Delta v_{nQ} \end{bmatrix}^T$,

$$\mathbf{A_{line}} = \begin{bmatrix} -\dfrac{R_{lik}}{L_{lik}} & \omega_0 \\ -\omega_0 & -\dfrac{R_{lik}}{L_{lik}} \end{bmatrix} \quad \mathbf{B_{line1}} = \begin{bmatrix} \dfrac{1}{L_{lik}} & 0 \\ 0 & \dfrac{1}{L_{lik}} \end{bmatrix},$$

$$\mathbf{B_{line2}} = \begin{bmatrix} -\dfrac{1}{L_{lik}} & 0 \\ 0 & -\dfrac{1}{L_{lik}} \end{bmatrix}, \ \mathbf{B_{\omega li}} = \begin{bmatrix} I_{lik0Q} \\ -I_{lik0D} \end{bmatrix}.$$

The $\Delta\omega_{ref}$ corresponds to the reference angular frequency from the reference DG unit. While, I_{lik0D} and I_{lik0Q} represent the initial condition of line in common D and Q axis reference frame, respectively.

Coupling between DG units, lines impedance and load is provided by local bus voltages equation as given in (1). By substituting (1) to (2), a complete state–space model of line impedance can be derived as shown in (3).

$$\boldsymbol{\Delta\dot{x}_{line}} = \{\mathbf{A_{line}} + R_N (\mathbf{B_{line1}} - \mathbf{B_{line2}})\} \boldsymbol{\Delta x_{line}}$$
$$+ \ \mathbf{B_{liDG}} \boldsymbol{\Delta i_{oDQ}} + \mathbf{B_{lilo}} \boldsymbol{\Delta i_{loDQ}} + \mathbf{B_{\omega li}} \Delta\omega_{ref} \qquad (3)$$

where $\mathbf{B_{liDG}} = \mathbf{B_{lilo}} = R_N (\mathbf{B_{line1}} - \mathbf{B_{line2}})$. The $\mathbf{B_{liDG}}$, $\mathbf{B_{lilo}}$ and $\mathbf{B_{li\omega}}$ represent connection matrices between line and corresponded DG units, load and reference DG respectively.

2.2. State-space model of static load

A load impedance model consists of load resistance (R_{lo}) and inductance (L_{lo}) is developed to present an aggregated load in MG. In general, state equation of the mth a central load is given by

$$\boldsymbol{\Delta\dot{x}_{lo}} = \mathbf{A_{lo}} \boldsymbol{\Delta x_{lo}} + \mathbf{B_{vlo}} \boldsymbol{\Delta v_{mDQ}} + \mathbf{B_{\omega lo}} \Delta\omega_{ref} \qquad (4)$$

where

$$\boldsymbol{\Delta x_{lo}} = \begin{bmatrix} \Delta i_{lomD} & \Delta i_{lomQ} \end{bmatrix}^T, \ \mathbf{A_{lo}} = \begin{bmatrix} -\dfrac{R_{lom}}{L_{lom}} & \omega_0 \\ -\omega_0 & -\dfrac{R_{lom}}{L_{lom}} \end{bmatrix},$$

$$\mathbf{B_{vlo}} = \begin{bmatrix} -\dfrac{1}{L_{lom}} & 0 \\ 0 & -\dfrac{1}{L_{lom}} \end{bmatrix}, \ \mathbf{B_{\omega lo}} = \begin{bmatrix} I_{lomQ} \\ -I_{lomD} \end{bmatrix}.$$

R_{lom} and L_{lom} represent resistance and inductance of line respectively.

The coupling between load, DG unit and distribution line is represented by bus voltage equation as given in (1). By substituting (1) to (4), the load state equation can be rewritten as

$$\boldsymbol{\Delta\dot{x}_{lo}} = \{\mathbf{A_{lo}} + R_N \mathbf{B_{vlo}}\} \boldsymbol{\Delta x_{lo}} + \mathbf{B_{loDG}} \boldsymbol{\Delta i_{oDQ}}$$
$$+ \ \mathbf{B_{loli}} \boldsymbol{\Delta i_{liDQ}} + \mathbf{B_{\omega lo}} \Delta\omega_{ref} \qquad (5)$$

where $\mathbf{B_{loDG}} = \mathbf{B_{loli}} = R_N \mathbf{B_{vlo}}$. The $\mathbf{B_{loDG}}$, $\mathbf{B_{loli}}$ and $\mathbf{B_{\omega lo}}$ represent connection matrices between load and corresponded DG units, line and reference DG respectively.

2.3. State-space model of bio-diesel generator (BDG)

The BDG is modelled as a permanent-magnet synchronous generator. In this research, the BDG is integrated to the hybrid MG as a reference DG unit which is responsible for providing a synchronization signal for other DG units and ensures the balanced condition of power generation and power consumption when there is a shortfall of energy from RES based DG units. The state–space model of BDG is derived from [18,19].
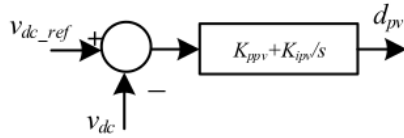
Fig. 2. DC/DC converter control.

State variables of the BDG involved two q axis (i_{kq12}) and one d axis (i_{kd}) rotor currents, stator current (i_{sdq}) and field winding currents (i_{fd}). Input variables are presented as mechanical torque (T_{MDE}), field winding (v_{fd}) and stator (v_{sdq}) voltage. The state–space model of BDG is then completed with mechanical equations of the turbine and electromagnetic torque. Output variables of the BDG are stator current and reference angular frequency (ω_{ref}). Linearized state–space model of BDG is given in (6).

$$\Delta \dot{x}_{BDEG} = A_{BDG} \Delta x_{BDG} + B_{BDG} \Delta u_{BDG} + B_{vBDG} \Delta v_{bDQ}$$

$$\begin{bmatrix} \Delta i_{sD} \\ \Delta i_{sQ} \\ \Delta \omega_{ref} \end{bmatrix} = \begin{bmatrix} C_{BDG1} \\ C_{BDG2} \end{bmatrix} \Delta x_{BDG} \qquad (6)$$

where $\Delta x_{BDG} = \begin{bmatrix} \Delta i_{sd} & \Delta i_{sq} & \Delta i_{fd} & \Delta i_{kd} & \Delta i_{kq1} & \Delta i_{kq2} & \Delta \omega_{ref} & \Delta \delta_{DE} \end{bmatrix}^T$, $\Delta u_{BDG} = \begin{bmatrix} \Delta v_{fd} & T_{MDE} \end{bmatrix}^T$, $\Delta v_{bDQ} = \begin{bmatrix} \Delta v_{bD} & \Delta v_{bQ} \end{bmatrix}^T$, $C_{BDG1} = \begin{bmatrix} 1 & 0 & 0_{1\times 6} \\ 0 & 1 & 0_{1\times 6} \end{bmatrix}$, $C_{BDG2} = \begin{bmatrix} 0_{1\times 6} & 1 & 0 \end{bmatrix}$. B_{BDG} represents input matrix for BDG corresponding to field voltage and mechanical torque. While B_{vBDG} represents input matrix of BDG related to stator voltage. A detailed presentation of B_{BDG} and B_{vBDG} are derived from [18,19].

The local bus voltage of BDG based DG unit is determined by using (1). Substitution of (1) into (6) yields a complete state–space equation of the BDG. Hence, state equation of BDG can be rewritten as

$$\Delta \dot{x}_{BDG} = (A_{BDG} + R_N B_{vBDG} C_{BDG1}) \Delta x_{BDG} + B_{BDG} \Delta u_{BDG}$$
$$+ B_{BDGline} \Delta x_{line} + B_{BDGload} \Delta x_{load} \qquad (7)$$

where $A_{BDG\_DG} = A_{BDG} + R_N B_{vBDG} C_{BDG1}$, $B_{BDGline} = R_N B_{vBDG}$, $B_{BDGlaod} = R_N B_{vBDG}$.

2.4. State-space model of two-stages PV system

Small-signal model of the two-stage PV system consists of PV array is modelled as constant DC voltage, DC/DC and DC/AC power converter [15]. Average model of DC/DC with input current (i_b), output current (i_s) and output voltage (v_b) state variables is derived from [20,21]. While DC/AC inverter model comprising of DC link voltage (v_{dc}), inverter current (i_{invdq}), output current (i_{odq}), and output voltage (v_{odq}) state variables is adapted from [21,22].

The proposed controllers for the two-stage PV system are comprising of input and grid-side power electronic devices controllers are presented in Figs. 2 and 3 respectively. Regulation of varying input DC voltage from PV array can be handled by DC/DC converter. Afterward, conditioned DC voltage is fed to the DC/AC inverter for providing power regulation and maintaining stable output voltage. Regulation of DC side input voltage of the DC/AC inverter are realized by adjusting duty cycle (d_{pv}) of DC/DC boost converter.

Auxiliary state equation (ρ_{pv}) of the proposed DC/DC controller loop is given by

$$\frac{d\Delta \rho_{pv}}{dt} = v_{dc\_ref} - v_{dc}. \qquad (8)$$

The controller generates a control signal for DC/DC converter. The state–space equation of DC/DC controller is given in (9).

$$\Delta \dot{\rho}_{pv} = [0] \Delta \rho_{pv} + \begin{bmatrix} 1 & -1 \end{bmatrix} \begin{bmatrix} \Delta v_{dc\_ref} \\ v_{dc} \end{bmatrix}$$
$$\Delta d_{pv} = \begin{bmatrix} K_{ipv} \end{bmatrix} \Delta \rho_{pv} + \begin{bmatrix} K_{ppv} & -K_{ppv} \end{bmatrix} \begin{bmatrix} \Delta v_{dc\_ref} \\ v_{dc} \end{bmatrix} \qquad (9)$$

where (Δv_{dc_ref}) represents the DC link reference voltage.

Controller of DC/AC grid-side inverter in Fig. 3 can be divided into droop control, outer voltage and inner current control loops [17,23]. Droop control method is employed to establish a power sharing for each DG unit. The instantaneous output power in a certain operating point is determined by linearizing the calculated instantaneous power as given by the following equations:

$$\Delta p = I_{od} \Delta v_{od} + I_{oq} \Delta v_{oq} + V_{od} \Delta i_{od} + V_{oq} \Delta i_{oq}$$
$$\Delta q = I_{oq} \Delta v_{od} - I_{od} \Delta v_{oq} - V_{oq} \Delta i_{od} + V_{od} \Delta i_{oq}. \qquad (10)$$

The average active (ΔP) and reactive (ΔQ) power are determined by employing first order low pass filter to the linearized
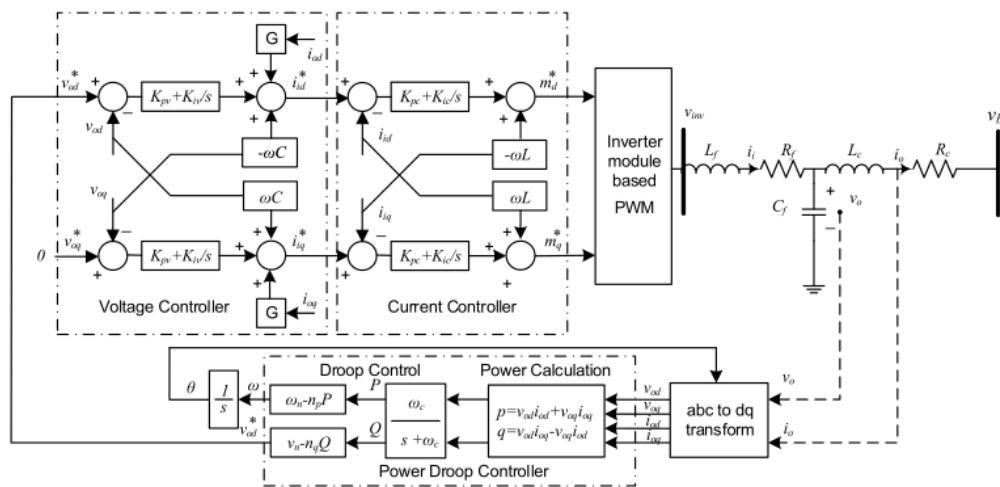

Fig. 3. Droop control of PV system DC/AC inverter [17].

instantaneous power as follows

$$\frac{d\Delta P}{dt} = \omega_c \left\{ I_{od}\Delta v_{od} + I_{oq}\Delta v_{oq} + V_{od}\Delta i_{od} + V_{oq}\Delta i_{oq} \right\} - \omega_c \Delta P$$
$$\frac{d\Delta Q}{dt} = \omega_c \left\{ I_{oq}\Delta v_{od} - I_{od}\Delta v_{oq} - V_{oq}\Delta i_{od} + V_{od}\Delta i_{oq} \right\} - \omega_c \Delta Q \tag{11}$$

where ω_c represent cut off frequency of the low pass filter.

System frequency (ω) and active power sharing are set by active power droop gain (n_p). While reference of d-axis voltage (v_{dq}^*) and reactive power sharing is determined by reactive power droop gain (n_q). It is assumed that q-axis component of voltage magnitude reference (Δv_{oq}^*) is zero. In most of the cases, output impedance of the inverter is inductive around the fundamental frequency [24]. Hence the reference frequency and voltage are given by the following equations:

$$\omega = \omega_n - n_p\Delta P$$
$$v_{od}^* = V_n - n_q\Delta Q \tag{12}$$

where ω_n and V_n represent nominal values of angular frequency and voltage respectively.

Phase angle (δ) between individual inverter reference frame and the common reference frame is determined from integral operation of the angular frequency (ω) [17]. By substituting (11) to (12), state–space equation of the droop controller can be determined as given in (13).

$$\begin{bmatrix} \Delta\dot{\delta} \\ \Delta\dot{p} \\ \Delta\dot{q} \end{bmatrix} = \begin{bmatrix} 0 & 0 & 0 \\ 0 & -\omega_c & 0 \\ 0 & 0 & -\omega_c \end{bmatrix} \begin{bmatrix} \Delta\delta \\ \Delta p \\ \Delta q \end{bmatrix}$$
$$+ \begin{bmatrix} 0 & 0 & 0 & 0 \\ \omega_c I_{od} & \omega_c I_{oq} & \omega_c V_{od} & \omega_c V_{oq} \\ \omega_c I_{oq} & -\omega_c I_{od} & -\omega_c V_{oq} & \omega_c V_{od} \end{bmatrix} \begin{bmatrix} \Delta v_{odq} \\ \Delta i_{odq} \end{bmatrix} \tag{13}$$

$$\begin{bmatrix} \Delta\omega \\ \Delta v_{odq}^* \end{bmatrix} = \begin{bmatrix} 0 & -n_p & 0 \\ 0 & 0 & -n_q \\ 0 & 0 & 0 \end{bmatrix} \begin{bmatrix} \Delta\delta \\ \Delta p \\ \Delta q \end{bmatrix}.$$

The obtained reference values from the power droop control are employed as input for voltage control loop. Auxiliary state equations (φ_d, φ_q) of voltage control loop is given by (14).

$$\frac{d\varphi_d}{dt} = v_{od}^* - v_{od}, \quad \frac{d\varphi_q}{dt} = v_{oq}^* - v_{oq}. \tag{14}$$

The algebraic equations of reference currents are determined as given by the following equations.

$$\Delta i_{id}^* = G\Delta i_{od} - \omega_n C_f \Delta v_{oq} + K_{pv}\left(\Delta v_{od}^* - \Delta v_{od}\right) + K_{iv}\Delta\varphi_d$$
$$\Delta i_{iq}^* = G\Delta i_{oq} + \omega_n C_f \Delta v_{od} + K_{pv}\left(\Delta v_{oq}^* - \Delta v_{oq}\right) + K_{iv}\Delta\varphi_q. \tag{15}$$

The linearized state equations of voltage control are derived from auxiliary state equation in (14) and the algebraic equations of the reference currents in (15) as given by (16).

$$\begin{bmatrix} \Delta\dot{\varphi}_d \\ \Delta\dot{\varphi}_q \end{bmatrix} = [0] \begin{bmatrix} \Delta\varphi_d \\ \Delta\varphi_q \end{bmatrix} + \begin{bmatrix} 1 & 0 & -1 & 0 \\ 0 & 1 & 0 & -1 \end{bmatrix} \begin{bmatrix} \Delta v_{odq}^* \\ \Delta v_{odq} \end{bmatrix} \tag{16}$$

$$\begin{bmatrix} \Delta i_{id}^* \\ \Delta i_{iq}^* \end{bmatrix} = \begin{bmatrix} K_{iv} & 0 \\ 0 & K_{iv} \end{bmatrix} \begin{bmatrix} \Delta\varphi_d \\ \Delta\varphi_q \end{bmatrix}$$

$$+ \begin{bmatrix} K_{pv} & 0 & -K_{pv} & -\omega_n C_f & G & 0 \\ 0 & K_{pv} & \omega_n C_f & -K_{pv} & 0 & G \end{bmatrix} \begin{bmatrix} \Delta v_{odq}^* \\ \Delta v_{odq} \\ \Delta i_{odq} \end{bmatrix}.$$

The proportional and integral gains of voltage control loop are presented by K_{pv} and K_{iv} respectively. While, feed forward gain control is stated as G.

Output variables from the voltage control are then applied to the inner current controller as reference values. Auxiliary state equations (β_d, β_q) of the current control loop as given by (17).

$$\frac{d\beta_d}{dt} = i_{id}^* - i_{id}, \quad \frac{d\beta_q}{dt} = i_{iq}^* - i_{iq}. \tag{17}$$

The algebraic equation of current controller loop related to inverter modulation index is given by the following equation

$$m_d^* = -\omega_n L_f \Delta i_{iq} + K_{pc}\left(\Delta i_{id}^* - \Delta i_{id}\right) + K_{ic}\Delta\beta_d$$
$$m_q^* = \omega_n L_f \Delta i_{id} + K_{pc}\left(\Delta i_{iq}^* - \Delta i_{iq}\right) + K_{ic}\Delta\beta_q. \tag{18}$$

The linearized state equations of current control are derived from auxiliary state equation in (17) and the algebraic equations of the modulation index in, (18) as given by (19).

$$\begin{bmatrix} \Delta\dot{\beta}_d \\ \Delta\dot{\beta}_q \end{bmatrix} = [0] \begin{bmatrix} \Delta\beta_d \\ \Delta\beta_q \end{bmatrix} + \begin{bmatrix} 1 & 0 & -1 & 0 \\ 0 & 1 & 0 & -1 \end{bmatrix} \begin{bmatrix} \Delta i_{idq}^* \\ \Delta i_{idq} \end{bmatrix}$$

$$\begin{bmatrix} \Delta m_d^* \\ \Delta m_q^* \end{bmatrix} = \begin{bmatrix} K_{ic} & 0 \\ 0 & K_{ic} \end{bmatrix} \begin{bmatrix} \Delta\beta_d \\ \Delta\beta_q \end{bmatrix} \tag{19}$$

$$+ \begin{bmatrix} K_{pc} & 0 & -K_{pc} & -\omega_n L_f \\ 0 & K_{pc} & \omega_n L_f & -K_{pc} \end{bmatrix} \begin{bmatrix} \Delta i_{idq}^* \\ \Delta i_{idq} \end{bmatrix}.$$

where, the proportional and integral gains of current control loop are presented by K_{pc} and K_{ic} respectively.

A complete model of PV system is determined by combining state equations of DC/DC and DC/AC in [21,25]. These converter models are then integrated into state–space equations of the DC link (9), power droop (13), voltage (16) and current (19) controllers. Eighteen state variables are considered to obtain a detailed model of two-stages PV based DG unit. Linearized state–space model of two-stages PV is given by

$$\Delta\dot{x}_{pv} = A_{pv}\Delta x_{pv} + B_{pv}\Delta u_{pv} + B_{vpv}\Delta v_{bpv} + B_{\omega pv}\Delta\omega_{ref}$$
$$\Delta i_{odq} = \begin{bmatrix} 0_{2\times16} & I_{2\times2} \end{bmatrix} \Delta x_{pv} \tag{20}$$

where

$$u_{pv} = \begin{bmatrix} \Delta v_g & \Delta v_{dc}^* \end{bmatrix}^T, \quad \Delta v_{bpv} = \begin{bmatrix} \Delta v_{bpvd} & \Delta v_{bpvq} \end{bmatrix}^T,$$

$$\Delta x_{pv} = \begin{bmatrix} \Delta i_b & \Delta i_s & \Delta v_b & \Delta v_{dc} & \Delta\rho_{pv} & \Delta\delta_{pv} & \Delta p_{pv} & \Delta q_{pv} & \Delta\varphi_{pvd} & \Delta\varphi_{pvq} \\ \Delta\beta_{pvd} & \Delta\beta_{pvq} & \Delta i_{id} & \Delta i_{iq} & \Delta v_{od} & \Delta v_{oq} & \Delta i_{od} & \Delta i_{oq} \end{bmatrix}^T$$

$$B_{pv} = \begin{bmatrix} \frac{1}{L_s} & K_{ppv}(I_{b0}R_{cb} - I_{s0}R_{cb} + V_{b0}) \\ 0 & \frac{L_b}{K_{ppv}I_{b0}R_b} \\ 0 & \frac{L_s}{K_{ppv}I_{b0}} \\ 0 & C_b \\ 0_{15\times1} & 0_{15\times1} \end{bmatrix},$$

$$B_{vpv} = \begin{bmatrix} 0_{16\times1} & 0_{16\times1} \\ -\frac{1}{L_c} & 0 \\ 0 & -\frac{1}{L_c} \end{bmatrix}, \quad B_{\omega pv} = \begin{bmatrix} 0_{5\times1} \\ -1 \\ 0_{12\times1} \end{bmatrix}.$$

The synchronization signal for PV based DG unit is provided by BDG which is presented by $\Delta\omega_{ref}$. By substituting $\Delta\omega_{ref}$ values as given in (6), the state equations of PV based DG unit can be rewritten as

$$\Delta\dot{x}_{pv} = A_{pv}\Delta x_{pv} + B_{pv}\Delta u_{pv} + B_{vpv}\Delta v_{bpv} + B_{\omega pv}C_{BDG2}\Delta x_{BDG}$$
$$\Delta i_{odq} = \begin{bmatrix} 0_{2\times16} & I_{2\times2} \end{bmatrix} \Delta x_{pv}. \tag{21}$$
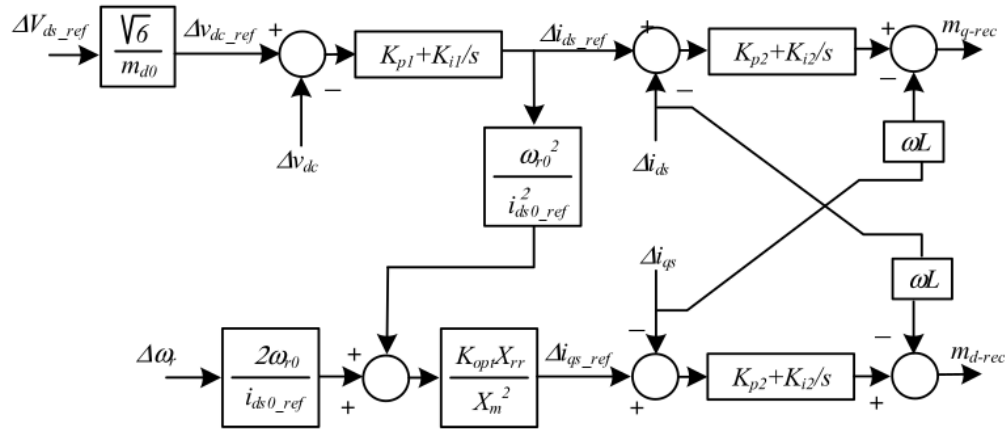
Fig. 4. FOC method for generator side converter [18,28].

Output currents of PV system have to be aligned with common reference frame as given by

$$\Delta \mathbf{i_{opvDQ}} = \mathbf{C_{pvDQ}} \Delta \mathbf{x_{pv}} \tag{22}$$

where $\mathbf{C_{pvDQ}} = \begin{bmatrix} 0_{2\times5} & \mathbf{T_{c\delta}} & 0_{2\times10} & \mathbf{T_f} \end{bmatrix}$.

The local bus voltage is one of the input variables for the state–space equations of PV based DG unit. Transformation of bus voltage variables from common to individual reference frame can be conducted by substituting (1) to (21) as given by

$$\begin{bmatrix} v_{bpvd} \\ v_{bpvq} \end{bmatrix} = \mathbf{T_f}^{-1} R_N \mathbf{C_{pvDQ}} \Delta \mathbf{x_{pv}} + \mathbf{T_{v\delta}} \begin{bmatrix} \Delta \delta_{pv} \end{bmatrix} - \mathbf{T_f}^{-1} R_N \begin{bmatrix} \Delta \mathbf{i_{loDQ}} \end{bmatrix}$$
$$+ \mathbf{T_f}^{-1} R_N \left\{ \begin{bmatrix} \Delta \mathbf{i_{liDQ}} \end{bmatrix}_{in} - \begin{bmatrix} \Delta \mathbf{i_{liDQ}} \end{bmatrix}_{out} \right\}. \tag{23}$$

By substituting (22) and (23) into (21) and considering that the $\Delta \delta_{pv}$ part has been integrated to the state matrix of PV based DG unit, the complete state–space model of two-stages PV based DG can be stated as

$$\dot{\Delta \mathbf{x_{pv}}} = \mathbf{A_{PV\_DG}} \Delta \mathbf{x_{pv}} + \mathbf{B_{pv}} \Delta \mathbf{u_{pv}} + \mathbf{B_{pvline}} \Delta \mathbf{x_{line}}$$
$$+ \mathbf{B_{pvload}} \Delta \mathbf{x_{load}} + \mathbf{B_{pv\_BDG}} \Delta \mathbf{x_{BDG}} \tag{24}$$

$$\Delta \mathbf{i_{opvDQ}} = \mathbf{C_{pvDQ}} \Delta \mathbf{x_{pv}}$$

where $\mathbf{A_{PV\_DG}} = \mathbf{A_{pv}} + R_N \mathbf{T_f}^{-1} \mathbf{B_{vpv}} \mathbf{C_{pvDQ}}$, $\mathbf{B_{pvline}} = R_N \mathbf{T_f}^{-1} \mathbf{B_{vpv}}$, $\mathbf{B_{pvload}} = R_N \mathbf{T_f}^{-1} \mathbf{B_{vpv}}$, $\mathbf{B_{pv\_BDG}} = \mathbf{B_{\omega pv}} \mathbf{C_{BDG2}}$.

2.5. State-space model of fully rated WECS

The fully rated WECS mainly consists of a wind turbine, induction or synchronous generator, back to back AC/DC/AC inverter and associated controllers. The two-stages AC/DC and DC/AC converter system facilitate the interface between generator and grid side of fully rated WECS while providing decoupling between those two elements. Hence, for small variation of wind power, the dynamics from the generator side due to wind fluctuation will not influence the dynamic of the grid. Moreover, the interfacing power electronic device is enabled to facilitate the variable speed operation capability of the generator which allows the effective regulation of voltage and power output [26]. Small-signal model of back to back AC/DC/AC inverter is obtained from integration of the subsystem in [22,27] and [25]. While, the linearized induction generator model is derived from [18,19]. A complete model of fully-rated WECS is determined by integrating the WECS state–space model in [15] with its associated controller. The controllers in fully-rated WECS is comprising of generator-side AC/DC converter and grid-side DC/AC inverter controllers.

Flux oriented control (FOC) strategy as shown in Fig. 4 is applied to the generator-side AC/DC converter to facilitate variable speed operation of induction generator, maintain generator voltage stability and perform DC link voltage regulation [28].

Reference of DC link voltage is determined from d-axis stator voltage reference value and nominal modulation index of AC/DC converter as given by [29]:

$$\Delta v_{dc\_ref} = \frac{\sqrt{6}}{m_{d0\_rec}} \Delta v_{ds\_ref}. \tag{25}$$

The calculated reference values of DC link voltage is then compared with the measured DC link voltage and regulated through PI controller. Auxiliary variables (γ) of the corresponded control loop is denoted by

$$\frac{d\gamma}{dt} = \Delta v_{dc\_ref} - \Delta v_{dc} \rightarrow \frac{d\gamma}{dt} = \frac{\sqrt{6}}{m_{d0}} \Delta v_{ds\_ref} - \Delta v_{dc}. \tag{26}$$

State-space equation corresponded to the d-axis current reference (Δi_{ds}^*) can be stated as

$$\begin{bmatrix} \dot{\Delta \gamma} \end{bmatrix} = [0] \Delta \gamma + [-1] \Delta v_{dcout} + \begin{bmatrix} \frac{\sqrt{6}}{m_{d0}} \end{bmatrix} \Delta v_{ds\_ref}$$
$$\Delta i_{ds}^* = [K_{i1}] \Delta \gamma + [-K_{p1}] \Delta v_{dcout} + \begin{bmatrix} \frac{\sqrt{6}}{m_{d0}} \end{bmatrix} \Delta v_{ds\_ref}. \tag{27}$$

The quadrature axis, q reference current (Δi_{qs}^*) is derived from torque-speed characteristic curve [18]. Electromagnetic torque equation can be simplified by assuming that rotor flux of induction generator is aligned to the direct axis ($\psi = 0$) and optimal operation of a wind turbine is attained [28]. The linearized q-axis reference current can be stated as

$$\Delta i_{qs}^* = \left(\frac{2\omega_{r0} K_{opt} X_{rr}}{i_{d0s}^* X_m^2} \right) \Delta \omega_r + \left(\frac{K_{i1} K_{opt} \omega_{r0}^2 X_{rr}}{\left(i_{d0s}^*\right)^2 X_m^2} \right) \Delta \gamma$$
$$- \left(\frac{K_{p1} K_{opt} \omega_{r0}^2 X_{rr}}{\left(i_{d0s}^*\right)^2 X_m^2} \right) \Delta v_{dcout} + \left(\frac{K_{p1} K_{opt} \omega_{r0}^2 X_{rr} \sqrt{6}}{\left(i_{d0s}^*\right)^2 X_m^2 m_{d0}} \right) \Delta v_{ds\_ref}. \tag{28}$$

Reference currents are compared to measured dq axis stator current and regulated by PI controller to generate a control signal for AC/DC converter (m_{dq}^*). Auxiliary variables (ρ_{wdq}) for calculating modulation indices of the AC/DC converter is denoted by

$$\frac{d\rho_{wd}}{dt} = i_{sd}^* - i_{sd}, \quad \frac{d\rho_{wq}}{dt} = i_{sq}^* - i_{sq}. \tag{29}$$

By integrating (27)–(29), state–space equations of FOC are given by

$$
\begin{bmatrix} \Delta\dot{\rho}_{wd} \\ \Delta\dot{\rho}_{wq} \end{bmatrix} = \begin{bmatrix} 0 & 0 \\ 0 & 0 \end{bmatrix} \begin{bmatrix} \Delta\rho_{wd} \\ \Delta\rho_{wq} \end{bmatrix}
$$
$$
+ \mathbf{B_{1FOC}} \begin{bmatrix} i_{sd} \\ i_{sq} \\ \Delta\gamma \\ \Delta v_{dc} \\ \Delta\omega \end{bmatrix} + \mathbf{B_{2FOC}} \begin{bmatrix} \Delta v_{sd}^* \end{bmatrix}
$$
$$
\begin{bmatrix} \Delta m_{1d} \\ \Delta m_{1q} \end{bmatrix} = \begin{bmatrix} K_{i2} & 0 \\ 0 & K_{i2} \end{bmatrix} \begin{bmatrix} \Delta\rho_{wd} \\ \Delta\rho_{wq} \end{bmatrix}
$$
$$
+ \mathbf{D_{FOC1}} \begin{bmatrix} \Delta i_{sd}^* \\ \Delta i_{sq}^* \\ \Delta i_{sd} \\ \Delta i_{sq} \end{bmatrix} + \mathbf{D_{FOC2}} \begin{bmatrix} \Delta\omega_r \end{bmatrix} + \mathbf{D_{FOC3}} \begin{bmatrix} \Delta v_{sd}^* \end{bmatrix}
$$
(30)

where

$$
\mathbf{B_{1FOC}} = \begin{bmatrix} -1 & 0 & K_{i1} & -K_{p1} & 0 \\ 0 & -1 & \dfrac{K_{i1}K_{opt}\omega_{r0}^2 X_r}{\left(i_{sd0}^*\right)^2 X_m^2} & -\dfrac{K_{p1}K_{opt}\omega_{r0}^2 X_r}{\left(i_{sd0}^*\right)^2 X_m^2} & \dfrac{2\omega_{r0}^2 K_{opt} X_r}{\left(i_{sd0}^*\right)^2 X_m^2} \end{bmatrix},
$$

$$
\mathbf{B_{FOC2}} = \begin{bmatrix} \dfrac{K_{p1}\sqrt{6}}{m_{1d0}} \\ \dfrac{K_{p1}K_{opt}\omega_{r0}^2 X_r \sqrt{6}}{\left(i_{sd0}^*\right)^2 X_m^2 m_{1d0}} \end{bmatrix},
$$

$$
\mathbf{D_{FOC1}} = \begin{bmatrix} -K_{p2} & -\omega L & K_{i1} & -K_{p1}K_{p2} \\ \omega L & -K_{p2} & \dfrac{K_{i1}K_{p2}K_{opt}\omega_{r0}^2 X_r}{\left(i_{sd0}^*\right)^2 X_m^2} & -\dfrac{K_{p1}K_{p2}K_{opt}\omega_{r0}^2 X_r}{\left(i_{sd0}^*\right)^2 X_m^2} \end{bmatrix},
$$

$$
\mathbf{D_{FOC2}} = \begin{bmatrix} 0 \\ \dfrac{2\omega_{r0}K_{p2}K_{opt} X_r}{\left(i_{sd0}^*\right)^2 X_m^2} \end{bmatrix}, \quad \mathbf{D_{FOC3}} = \begin{bmatrix} \dfrac{K_{i1}K_{p2}\sqrt{6}}{m_{1d0}} \\ \dfrac{K_{p1}K_{p2}K_{opt}\omega_{r0}^2 X_{rr}\sqrt{6}}{\left(i_{sd0}^*\right)^2 X_m^2 m_{1d0}} \end{bmatrix}.
$$

Similar control algorithm as in two-stage PV system is adopted in WECS DC/AC inverter control. A complete state–space model for fully rated WECS is then derived from the integration of induction generator model [18,19], AC/DC/AC inverter model [25,27], generator side (FOC) controller in (27) and (30), and grid side controller (13), (16) and (19). Twenty-eight state variables are considered to determine a detailed model of WECS-based DG unit. Linearized state equations of WECS are given by in (31).

$$
\Delta\dot{\mathbf{x}}_{\mathbf{w}} = \mathbf{A_w}\Delta\mathbf{x_w} + \mathbf{B_w}\Delta\mathbf{u_w} + \mathbf{B_{vw}}\Delta\mathbf{v_{bw}} + \mathbf{B_{\omega w}}\Delta\omega_{ref}
$$
$$
\Delta\mathbf{i_{owdq}} = \begin{bmatrix} 0_{2\times26} & \mathbf{I_{2\times2}} \end{bmatrix} \Delta\mathbf{x_w}
$$
(31)

where $\Delta\mathbf{u_w} = \begin{bmatrix} \Delta v_{sd} & \Delta v_{sq} & \Delta v_{rd} & \Delta v_{rq} & \Delta T_w & \Delta v_{sd}^* \end{bmatrix}^T$, $\Delta\mathbf{v_{bw}} = \begin{bmatrix} \Delta v_{bwd} & \Delta v_{bwq} \end{bmatrix}^T$,

$$
\Delta\mathbf{x_w} = \begin{bmatrix} \Delta i_{sd} & \Delta i_{sq} & \Delta i_{rd} & \Delta i_{rq} & \Delta\omega_r & \Delta\gamma & \Delta\rho_{wd} & \Delta\rho_{wq} \\ \Delta i_{1d} & \Delta i_{1q} & \Delta v_{din} & \Delta v_{qin} & \Delta v_{dcout} & \Delta\delta & \Delta p & \Delta q & \Delta\varphi_d & \Delta\varphi_q \\ \Delta\beta_d & \Delta\beta_q & \Delta i_s & \Delta v_{dc} & \Delta i_{lwd} & \Delta i_{lwq} & \Delta v_{owd} & \Delta v_{owq} & \Delta i_{owd} & \Delta i_{owq} \end{bmatrix}^T,
$$

$$
\mathbf{B_{vw}} = \begin{bmatrix} 0_{26\times1} & 0_{26\times1} \\ -\dfrac{1}{L_c} & 0 \\ 0 & -\dfrac{1}{L_c} \end{bmatrix}, \quad \mathbf{B_{\omega w}} = \begin{bmatrix} 0_{13\times1} \\ -1 \\ 0_{14\times1} \end{bmatrix}.
$$

While, the detailed presentation of $\mathbf{B_w}$ is derived from [18,19].

The synchronization signal for WECS based DG unit is provided by BDG which is presented by $\Delta\omega_{ref}$. By substituting $\Delta\omega_{ref}$ values as given in (6), the state equations of WECS based DG unit can be rewritten as

$$
\Delta\dot{\mathbf{x}}_{\mathbf{w}} = \mathbf{A_w}\Delta\mathbf{x_w} + \mathbf{B_w}\Delta\mathbf{u_w} + \mathbf{B_{vw}}\Delta\mathbf{v_{bw}} + \mathbf{B_{\omega w}}\mathbf{C_{BDG2}}\Delta\mathbf{x_{BDG}}
$$
$$
\Delta\mathbf{i_{owdq}} = \begin{bmatrix} 0_{2\times26} & \mathbf{I_{2\times2}} \end{bmatrix} \Delta\mathbf{x_w}.
$$
(32)

Output currents of WECS have to be aligned to the common reference frame to facilitate synchronization with other DG unit. The transformation of WECS output current from individual to common reference frame is given by

$$
\Delta\mathbf{i_{owDQ}} = \mathbf{C_{wDQ}}\Delta\mathbf{x_w}
$$
(33)

where $\mathbf{C_{wDQ}} = \begin{bmatrix} 0_{2\times13} & \mathbf{T_{c\delta}} & 0_{2\times12} & \mathbf{T_f} \end{bmatrix}$.

Similar procedure as in PV system is conducted to determine the connection between WECS, DE and line impedance. Complete state–space model of WECS can be stated as given by

$$
\Delta\dot{\mathbf{x}}_{\mathbf{w}} = \mathbf{A_{w\_DG}}\Delta\mathbf{x_w} + \mathbf{B_w}\Delta\mathbf{u_w} + \mathbf{B_{wline}}\Delta\mathbf{x_{line}}
$$
$$
+ \mathbf{B_{wload}}\Delta\mathbf{x_{load}} + \mathbf{B_{w\_BDG}}\Delta\mathbf{x_{BDG}}
$$
$$
\Delta\mathbf{i_{owDQ}} = \mathbf{C_{wDQ}}\Delta\mathbf{x_w}
$$
(34)

where $\mathbf{A_{w\_DG}} = \mathbf{A_w} + R_N\mathbf{T_f^{-1}}\mathbf{B_{vw}}\mathbf{C_{wDQ}}$, $\mathbf{B_{w\_BDG}} = \mathbf{B_{\omega w}}\mathbf{C_{BDG2}}$, $\mathbf{B_{wline}} = R_N\mathbf{T_f^{-1}}\mathbf{B_{vw}}$, $\mathbf{B_{wload}} = R_N\mathbf{T_f^{-1}}\mathbf{B_{vw}}$.

2.6. Comprehensive state–space model of hybrid MG, small-signal stability and modal interaction

The proposed modelling procedure can be expanded for constructing a MG system which is consisting of a number of DG units. In general, the detailed state equation of n DG units and one reference DG unit can be rewritten as

$$
\Delta\dot{\mathbf{x}}_{\mathbf{DG1}} = \mathbf{A_{DG1}}\Delta\mathbf{x_{DG1}} + \mathbf{B_{DG1}}\Delta\mathbf{u_{DG1}} + \mathbf{B_{DG1\_line}}\Delta\mathbf{x_{line}}
$$
$$
+ \mathbf{B_{DG1\_ref}}\Delta\mathbf{x_{DGref}} + \mathbf{B_{DG1\_lo}}\Delta\mathbf{x_{lo}}
$$
$$
\Delta\dot{\mathbf{x}}_{\mathbf{DG2}} = \mathbf{A_{DG2}}\Delta\mathbf{x_{DG2}} + \mathbf{B_{DG2}}\Delta\mathbf{u_{DG2}} + \mathbf{B_{DG2\_line}}\Delta\mathbf{x_{line}}
$$
$$
+ \mathbf{B_{DG2\_ref}}\Delta\mathbf{x_{DGref}} + \mathbf{B_{DG2\_lo}}\Delta\mathbf{x_{lo}}
$$
$$
\vdots = \vdots \quad \vdots \quad \vdots
$$
$$
\Delta\dot{\mathbf{x}}_{\mathbf{DGn}} = \mathbf{A_{DGn}}\Delta\mathbf{x_{DGn}} + \mathbf{B_{DGn}}\Delta\mathbf{u_{DGn}} + \mathbf{B_{DGn\_line}}\Delta\mathbf{x_{line}}
$$
$$
+ \mathbf{B_{DGn\_ref}}\Delta\mathbf{x_{DGref}} + \mathbf{B_{DGn\_lo}}\Delta\mathbf{x_{lo}}
$$
$$
\Delta\dot{\mathbf{x}}_{\mathbf{DGref}} = \mathbf{A_{DGref}}\Delta\mathbf{x_{DGref}} + \mathbf{B_{DGref}}\Delta\mathbf{u_{DGref}}
$$
$$
+ \mathbf{B_{DGref\_line}}\Delta\mathbf{x_{line}} + \mathbf{B_{DGref\_lo}}\Delta\mathbf{x_{lo}}
$$
(35)

where $\mathbf{A_{DGn}}$ and $\mathbf{A_{DGref}}$ represent state matrix of a particular and reference DG unit respectively. The input matrices of a particular and reference DG unit are presented by $\mathbf{B_{DGn}}$ and $\mathbf{B_{DGref}}$ respectively. Connections between a particular DG unit with the reference DG, distribution lines and load are stated by input matrices of $\mathbf{B_{DGn\_line}}$, $\mathbf{B_{DGn\_ref}}$ and $\mathbf{B_{DGn\_lo}}$ respectively. Moreover, the generic state–space equations of line impedance and load are derived from (3) and (5) respectively.

Considering that the n RES based DG unit, one reference DG unit supplied m number of loads through k line impedance model, the general small signal model of the MG system can be rewritten as

$$
\Delta\dot{\mathbf{x}}_{\mathbf{MG}} = \mathbf{A_{MG}}\Delta\mathbf{x_{MG}} + \mathbf{B_{MG}}\Delta\mathbf{u_{MG}}.
$$
(36)

where

$$
\Delta\mathbf{x_{MG}} = \begin{bmatrix} \Delta\mathbf{x_{DG1}} & \Delta\mathbf{x_{DG2}} & \cdots & \Delta\mathbf{x_{DGn}} & \Delta\mathbf{x_{DGref}} & \Delta\mathbf{x_{line}} & \Delta\mathbf{x_{load}} \end{bmatrix}^T,
$$
$$
\Delta\mathbf{u_{MG}} = \begin{bmatrix} \Delta\mathbf{u_{DG1}} & \Delta\mathbf{u_{DG2}} & \cdots & \Delta\mathbf{u_{ref}} \end{bmatrix}^T,
$$

Fig. 5. The test system of hybrid MG.
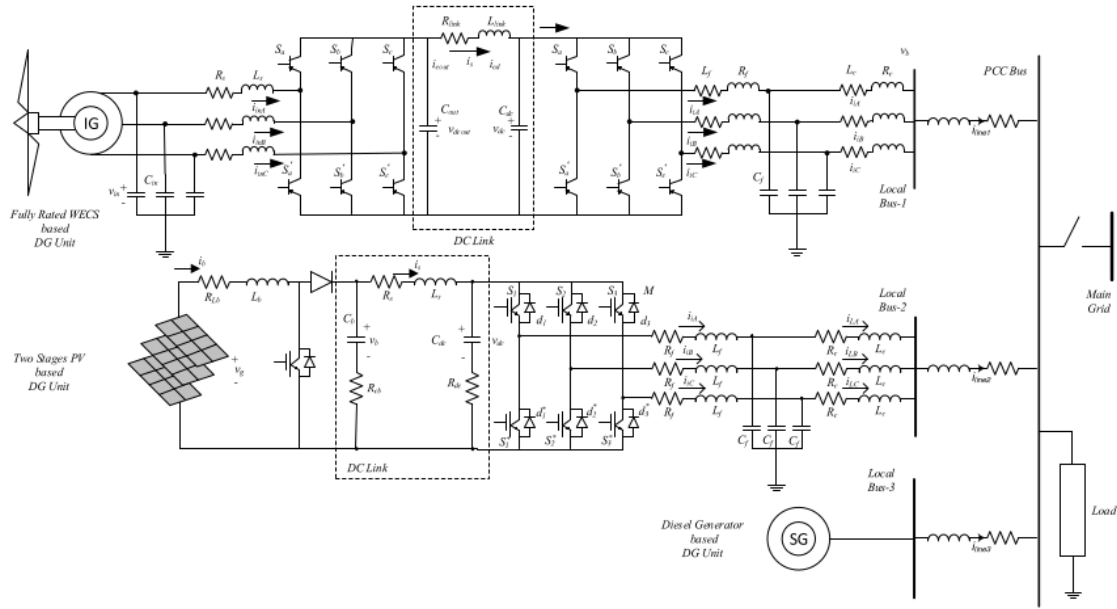
$$B_{MG} = \begin{bmatrix} B_{DG1} & 0 & 0 & 0 & 0 \\ 0 & B_{DG2} & 0 & 0 & 0 \\ 0 & 0 & \ddots & 0 & 0 \\ 0 & 0 & 0 & B_{DGn} & 0 \\ 0 & 0 & 0 & 0 & B_{DGref} \end{bmatrix},$$

$$A_{MG} = \begin{bmatrix} A_{DG1} & 0 & 0 & 0 & B_{DG1\_ref} & B_{DG1\_line} & B_{DG1\_lo} \\ 0 & A_{DG2} & 0 & 0 & B_{DG2\_ref} & B_{DG2\_line} & B_{DG2\_lo} \\ \vdots & \vdots & \ddots & \vdots & \vdots & \vdots & \vdots \\ 0 & 0 & 0 & A_{DGn} & B_{DGn\_ref} & B_{DGn\_line} & B_{DGn\_lo} \\ 0 & 0 & 0 & 0 & A_{DGref} & B_{DGref\_line} & B_{DGref\_lo} \\ B_{line\_DG1} & B_{line\_DG2} & \cdots & B_{line\_DGn} & B_{line\_DGref} & A_{line} & B_{lilo} \\ B_{lo\_DG1} & B_{lo\_DG2} & \cdots & B_{lo\_DGn} & B_{lo\_DGref} & B_{loli} & A_{load} \end{bmatrix}.$$

Eigenvalues analysis is carried out to analyse system small-signal stability. The system eigenvalues (λ) reveal important information corresponded to oscillatory frequency (f) and damping ratio (ζ) of the modes. Moreover, contributions of state variables are monitored through participation factor analysis.

The complex design of MG controller influences the dynamic behaviour of sensitive modes. The interaction between eigenvalues may happen since those two modes might be located closely. They approach each other and align with a certain point known as interaction or resonance point. Around a resonance point, the more oscillatory condition might be observed. Hence, the modal interaction could be a concern since it might be a precursor to system instability. As modal interaction happened, the engaged modes become very sensitive and depart oppositely to parameter variations.

3. Simulation results

A hybrid MG model consisting of three DG units; WECS, PV and BDG is investigated in this study as depicted in Fig. 5. Two-stage converter system comprising of DC/DC and DC/AC formed a PV based DG unit. While, typical fully rated WECS incorporating DC/AC/DC converter was selected due to its superior characteristics in providing full power conversion and variable generator speed

operation capability [28,30]. Mitigation of high order harmonics of DG units' output current and voltage are handled by interfaced low pass filter. BDG is connected as a reference DG unit which provides a synchronization signal for other DG units and additional power when the generated power from PV and WECS are not sufficient to supply the load. In the investigated MG system, three line-impedances are considered to connect each DG unit with the single load bus. Moreover, an aggregated static load is considered in this study.

It is expected that the detailed MG model would provide more accurate results correlated to the ability of the proposed model to capture various dynamic response from different RES based DG units (WECS, PV and BDG). On the other hand, it is difficult to observe the typical dynamic behaviours from different DG unit architectures using simplified model as presented in the literature [5,14,17,20,31–33]. The analysis of MG small signal stability using the simplified model results in similar dynamic responses for all the inverter based DG unit. Therefore, the simplified approach is not sufficient to present or to model a system with different type of RES based DG units.

3.1. Eigenvalues analysis

A complete state–space model of hybrid MG was constructed. The capacity of each DG unit in the proposed MG; WECS, PV and BDG, is 3 MVA which provides a power supply for 5 MW load through the distribution network. Parameters of WECS and DE were derived from [29] and [19] respectively. The parameters of power electronic devices, low pass filter and line impedance are presented in Appendix.

This study focused on low-frequency critical modes, which significantly affect the MG stability. The low-frequency critical eigenvalues are mainly originated from the power-sharing controller in the frequency range of 2–10 Hz [8,34]. According to participation factor analysis, active power, phase angle and reactive power state variables from PV and WECS contributed to modes of $\lambda_{42,43}$ and $\lambda_{45,46}$ respectively. It was also monitored that mode of $\lambda_{42,43}$ has a damping ratio of 17.68% while $\lambda_{45,46}$ is characterized by 4.13%
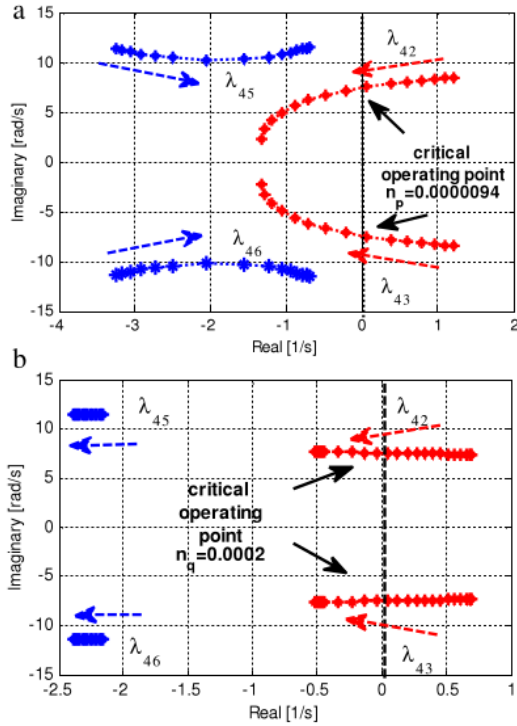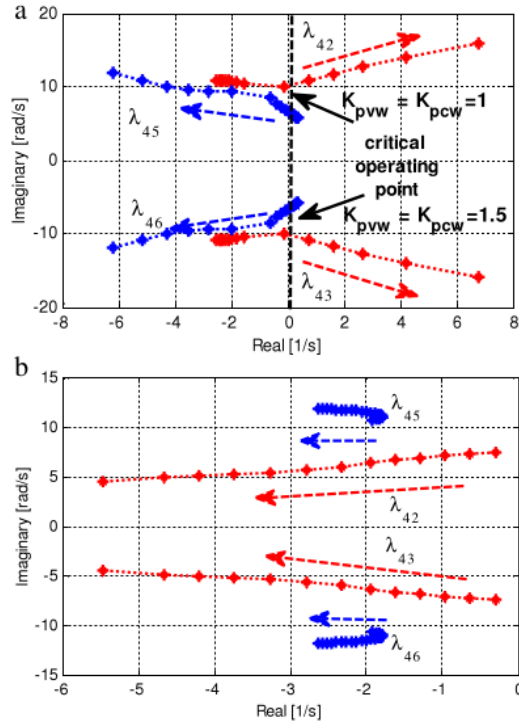
Fig. 6. Trajectories of sensitive modes when (a) active power droop gain (n_p) varied from 1.57×10^{-5} rad/s/W to 1.05×10^{-6} rad/s/W and (b) reactive power droop gain (n_q) varied from 4.2×10^{-4} V/Var to 8.8×10^{-5} V/Var.

Fig. 7. Trajectories of sensitive modes when proportional (K_{pvw}, K_{pcw}) (a) and integral (K_{ivw}, K_{icw}) (b) gains of WECS voltage and current controller were varied.

damping ratio. This indicated that the risk of instability from eigenvalues of $\lambda_{45,46}$ is higher than that from $\lambda_{42,43}$. Moreover, since the investigated modes were situated closely, similar state variables might participate in those neighbouring eigenvalues. It can be denoted that in this situation, the eigenvectors of the corresponded modes might be similar [35]. As a consequence, the interaction between those modes potentially occurred. The interaction event might lead to more oscillatory conditions which result in deterioration of system damping or even unstable situations.

Trajectories of sensitive modes from RES based DG unit under variations of gain control parameters are presented in this study. Small variation of droop gain, proportional and integral gain control in a certain range are considered. Fig. 6(a) shows root-locus of the investigated modes due to the variation of active-power droop gain (n_p) of PV and WECS. As n_p decreased, modes of $\lambda_{42,43}$ moved to the right, implies a deterioration of dynamic response. On the other hand, enhancement of oscillatory condition was monitored indicated by the left movement of $\lambda_{45,46}$. Oscillatory frequency of $\lambda_{45,46}$ drastically decreased from 7.408 rad/s or 1.17 Hz to 4.01 rad/s or 0.63 Hz at lower values of n_p. While the frequency of mode $\lambda_{42,43}$ did not change significantly around 10.682 rad/s or 1.701 Hz. Furthermore, it was suggested that stability could be maintained if droop gains were set more than 9.4×10^{-6} rad/s/W.

Trajectories of sensitive modes due to the variation of reactive power droop gain (n_q) s depicted in Fig. 6(b). Enhancement of system dynamic response was monitored, designated by extensive left movement of $\lambda_{45,46}$ across the imaginary axis. Critical mode of $\lambda_{42,43}$ was also influenced. The slight left motion of the $\lambda_{42,43}$ was observed during this variation. Moreover, system stability could be maintained if the n_q was tuned less than 2×10^{-4} V/Var.

Investigation of low-frequency critical modes was then conducted by a varying gain of WECS voltage (K_{pvw}, K_{ivw}) and current (K_{pcw}, K_{icw}) controller loops. As depicted in Fig. 7(a), eigenvalues of $\lambda_{42,43}$ departed toward left half plane due to K_{pvw} and K_{pcw} variations. Conversely, dynamic response of $\lambda_{45,46}$ deteriorated significantly as K_{pvw} and K_{pcw} were varied. From this variation, system stability boundary was determined. Stability could be maintained if K_{pvw} and K_{pcw} were tuned in the range of 1 to 1.5. Moreover, small-signal stability corresponded to DG units output power due to K_{ivw} and K_{icw} variations is shown in Fig. 7(b). As K_{ivw} and K_{icw} were varied the observed modes departed to the left. This indicated damping enhancements of corresponded eigenvalues.

In Fig. 8, different circumstances were observed as proportional (K_{pvpv}, K_{pcpv}) and integral (K_{ivpv}, K_{icpv}) gains of PV voltage and current control loops were varied. The trajectory of low-frequency critical modes under K_{pvpv} and K_{pcpv} variations is shown in Fig. 8(a). Primarily, the eigenvalues of $\lambda_{42,43}$ departed to the left-hand side. However, as the gain controller was continuously increased, the investigated modes of $\lambda_{42,43}$, start to move towards the imaginary axis, indicating deterioration of system dynamic response. On the other hand, only small movement of modes of $\lambda_{45,46}$ was monitored. Moreover, small-signal stability corresponding to DG unit output power due to K_{ivpv} and K_{icpv} variations is shown in Fig. 8(b). As K_{ivpv} and K_{icpv} were varied the observed modes departed to the left, indicating damping enhancements of the system. To maintain a stable condition of PV output power, K_{pvpv} and K_{pcpv} should be tuned more than 0.3 as depicted in Fig. 8(a). While, as shown in Fig. 8(b), the risk of instability potentially occurred when K_{ivpv} and K_{icpv} were set less than 2.

Dynamic features of power electronic devices were characterized by higher frequency of oscillation. The sensitive modes of these devices were represented by voltage and current of DC link
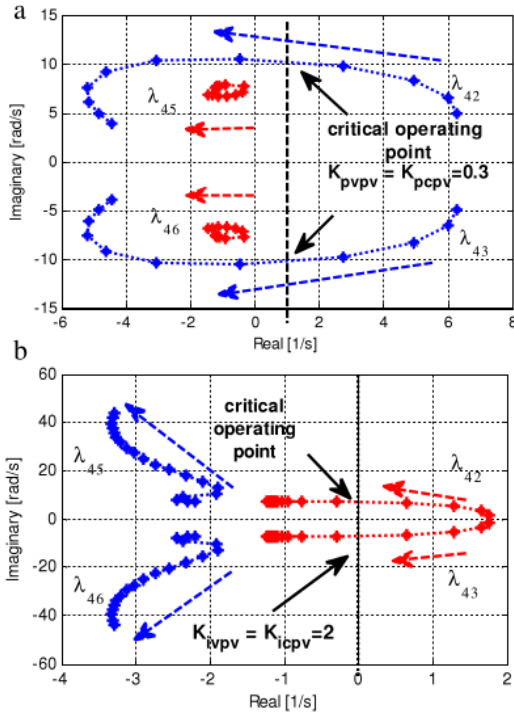
Fig. 8. Trajectories of modes when proportional (K_{pvpv}, K_{pcpv}) (a) and integral (K_{ivpv}, K_{icpv}) (b) gains of PV voltage and current controller were varied.

Fig. 9. Trajectories of DC link voltage and current in WECS when the proportional gain of FOC (K_{pFOC}) varied from 0.01 to 0.2.

Fig. 10. Trajectories of DC link voltage and current in PV system when DC link gain controller (K_{ppv}) varied from 0.001 to 0.004.

and inverter state variables. Fig. 9 represents root loci due to the variation of FOC gain. As the gain of the controller varied, the modes corresponded to DC link voltage and current from WECS ($\lambda_{20,21}$), drastically moved toward to imaginary axis, indicated deterioration of system stability. Moreover, it was also observed that system be unstable if the proportional gain of FOC (K_{pFOC}) was tuned above 0.15. Dynamic response of DC link voltage and current of PV ($\lambda_{26,27}$) due to the variation of proportional DC link control gain (K_{pDC}) is shown in Fig. 10. It was clearly seen that as K_{pDC} increased, system small-signal stability deteriorated severely. Instability possibly occurred when the K_{pDC} was tuned beyond 0.0032.

3.2. Time-domain simulation

Time domain simulations in MATLAB Simulink environment were conducted to validate previous eigenvalues analysis. Small perturbations of input variables associated with a voltage reference of WECS (v_{ds}^*) and PV (v_{dc}^*) controller were applied to excite sensitive modes.

Fig. 11 represents dynamic response of WECS and PV active power due to the variation of n_p. According to the previous eigenvalues analysis, at n_p of 7.32 × 10^6 rad/s/W, the output power of WECS and PV had an oscillatory frequency of 7.408 rad/s or 1.17 Hz and 10.758 rad/s or 1.71 Hz, respectively as shown in Fig. 11(a). Primarily, PV active power oscillated in the 0.58 s time period or 1.72 Hz. While WECS power output oscillated at 0.9 s time period or 1.1 Hz. Since eigenvalues related to PV output power has a higher damping ratio of 17.48%, the dynamic response subsided immediately. While lower frequency around 1.1 Hz from WECS modes persisted until the stable operating point was achieved.

The critical operating point was experienced when n_p was tuned at 9.35 × 10^6 rad/s/W as depicted in Fig. 11(b). At this
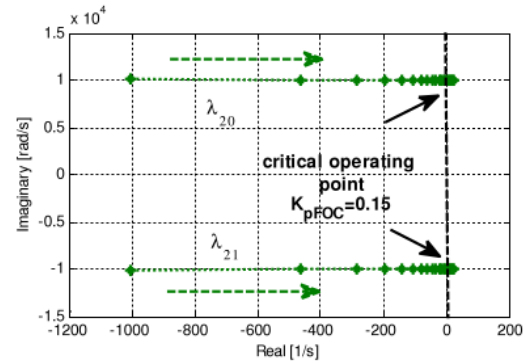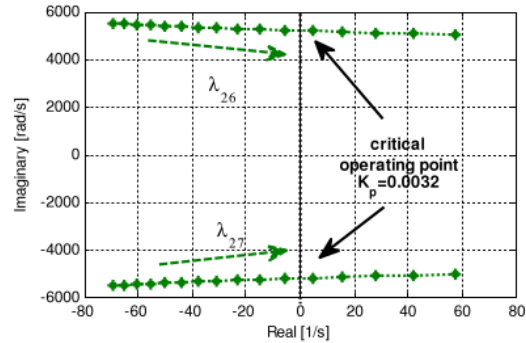
operating condition, WECS and PV active power oscillated continuously. Primarily, PV output power oscillated at 0.6 s time period or 1.67 Hz. According to root loci in Fig. 6(a), at the critical points, positions of $\lambda_{45,46}$ was closer to the imaginary axis than modes of $\lambda_{42,43}$, denote the less damped condition of $\lambda_{45,46}$ than $\lambda_{42,43}$. Hence, the oscillation associated to $\lambda_{42,43}$ dissolved immediately and then two modes started to oscillate together in the 0.9 s time period or 1.1 Hz.

3.3. Power sharing and small-signal stability

The dynamic behaviour of MG is not only influenced by the setting of gain parameters such as droop, voltage and current controller gain but also influenced by parameters of the converter, line impedances and load. Higher R/X ratio of line impedance result in more system damping hence it can enhance the MG dynamic response. Conversely, increasing line resistance value affects the accuracy of power-sharing and voltage profile within MG [8].

Converter parameters such as the inductance values and cut off frequency of low pass filter (LPF) also influenced the dynamic responses of MG. A compromise between enhancing dynamic system dynamic response and providing better harmonic rejection capability has to be considered in selecting the LPF parameters [36]. Even though converter and line parameters influenced the MG stability performance, those parameters can be considered constant according to their primary design. The presented work is focused on the investigation of oscillatory conditions in a MG system under different gain settings involving droop, voltage and current gain control settings. A detailed explanation of gain control impact on MG stability is important since MG mostly powered by RES with
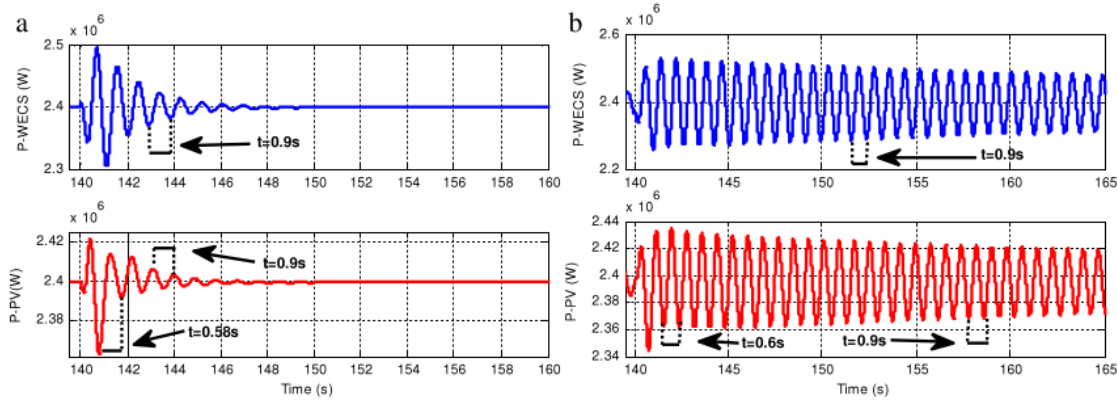
Fig. 11. WECS and PV active power at active droop gain (n_p) of (a) 7.32×10^{-6} and (b) 9.35×10^{-6}.
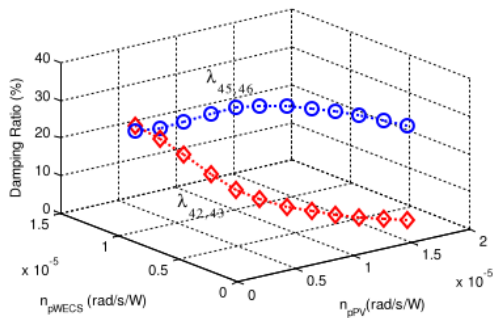

Fig. 12. The damping ratio of the low-frequency critical modes in different power sharing schemes.

fluctuating nature characteristic. Therefore, proper gain control adjustments and settings should be better understood to ensure accurate power-sharing and stable MG operation.

MG is demanded to deal with all possible power-sharing strategies. It was considered that generated active power from WECS and PV were varied by gradually adjusting active power droop gain in each DG unit. While lack of supplied power from those DG units is handled by BDG. In practice, minimum allowable output from BDG is around 30% of its nominal rating (under-loading operation of diesel engine less than 30% for extended periods can impact uptime and engine life). Therefore, in this study it is considered that the diesel engine generator is operated around 30%–50% of its nominal rating. Fig. 12 shows damping ratio of sensitive modes in different power sharing schemes. It was observed that at higher WECS and lower PV power-sharing, eigenvalues of $\lambda_{42,43}$ and $\lambda_{45,46}$ had 4.23% and 29.36% damping ratio respectively. MG dynamics response enhanced as power portion of WECS and PV were decreased and increased respectively. The damping ratio of $\lambda_{42,43}$ significantly enhanced to 23.11%. While damping ratio of modes of $\lambda_{45,46}$ decreased moderately to 21.86%.

Fig. 13 depicts MG dynamic responses associated with different power-sharing scheme among DG units. The presented result confirmed the previous eigenvalues analysis in Fig. 12. As shown in Fig. 13(a), when MG was operated with dominant power from WECS and 40% nominal rating of BDG (1.25 MW), less system damping was monitored. The less damping situation was reflected by more oscillatory condition when the MG was subjected to small disturbance. Fig. 13(b) presents equal contribution from WECS and PV based DG units with BDG was operated at 45% of its nominal

rating (1.33 MW). From this figure, it can be observed that more damped situation than in Fig. 13(a) was monitored. Enhancement of system damping was further monitored when dominant power contribution from PV and higher power injection from BDG (1.48 MW or 50% from its nominal rating) were considered, as shown in Fig. 13(c).

3.4. Modal interaction

The modal interaction could be a concern since it may cause a resonance phenomenon which deteriorated system stability. Interaction among neighbouring modes may emerge due to a variation of system parameter such as a gain controller, load changing and disturbance. Since modes of $\lambda_{42,43}$ and $\lambda_{45,46}$ situated closely, they could potentially interact. To investigate interaction scenarios, trajectories of the corresponded modes due to the variation of active power droop gain n_p in different WECS (K_{pvw}, K_{pcw}) and PV (K_{pvpv}, K_{pcpv}) voltage and current proportional gain tuning were investigated.

Fig. 14 shows trajectories of investigated modes in different K_{pvw}, K_{pcw} and K_{pvpv}, K_{pcpv} setting during n_p variation. It was obviously shown that with similar n_p variation, different gain setting significantly influenced the eigenvalues movements. It was observed in Fig. 14(a), primarily, two eigenvalues came closer and interacted when K_{pvw} and K_{pcw} were tuned at 1.04. Around interaction point, as marked by a circle, those two modes moved oppositely. Modes of λ_{42} departed to the left while λ_{45} moved towards the right side of complex the plane, indicated enhancement and deterioration of system stability respectively. A similar trend was observed in Fig. 14(b). It was shown that after the interaction, PV modes moved to the right remarkably. Moreover, for lower n_p, the corresponded modes be unstable. The modal interaction emerged at K_{pvpv} and K_{pcpv} setting of 0.35.

The effect of modal interaction on the oscillatory condition in a MG system is visualized in time domain simulation as presented in Fig. 15. The occurrence of modal interaction under variation of WECS gain control is depicted in Fig. 15(a). When proportional gains control of WECS (K_{pvw}, K_{pcw}) were tuned at 1.01, the more damped situation was observed. In this gain control setting, the two investigated modes were far away from each other. Therefore, modal interaction did not take place. As the gains control of WECS and PV were tuned at 1.04, the more oscillatory condition was observed. At those particular gain setting, the two modes become closer and start to interact. Around an interaction point, as marked by a circle in Fig. 14, the engaged modes were very sensitive to small parameter variations. When K_{pvw} and K_{pcw} were further
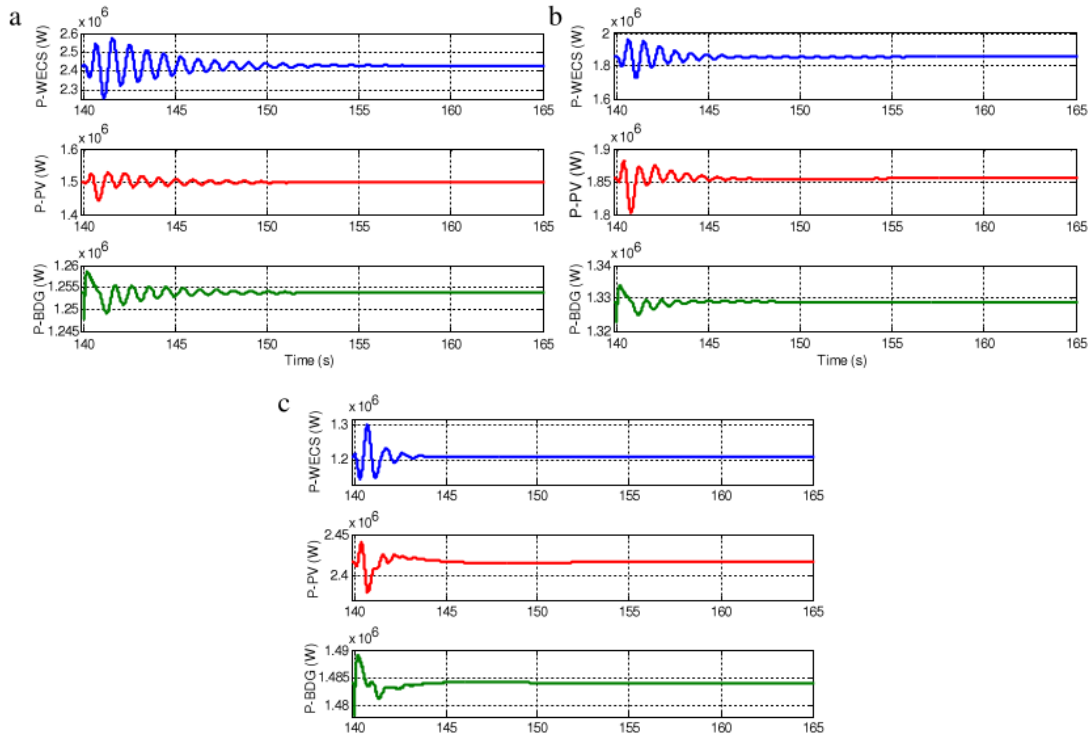
Fig. 13. Power sharing schemes in MG: (a) Dominant WECS, (b) Dominant PV and (c) Higher Contribution from BDG.
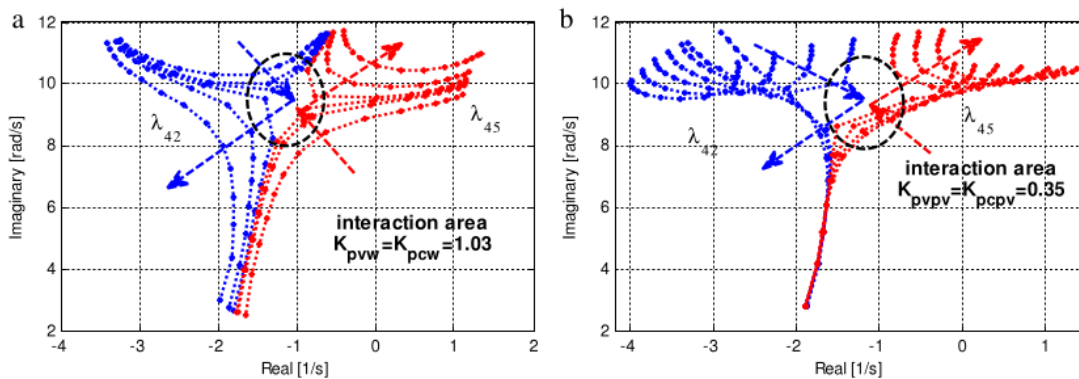

Fig. 14. Trajectories of modes due to the variation of active power droop gain in the various setting of (a) WECS and (b) PV control gains.

increased to 1.06, a significant deviation of the root-loci was monitored. The two modes departed oppositely. One of the interacting modes departed to the left, yielded an enhancement of system oscillatory condition. While the other modes significantly moved toward the right-hand side of the complex plane. Those low-frequency modes which related to PV based DG unit dominantly affected the system stability. As a consequence, more damped condition subsided immediately and replaced by the less damped situation with similar oscillatory frequency as modes of PV.

A similar situation was monitored when PV gains control (K_{pvpv}, K_{pcpv}) were varied. The occurrence of modal interaction under variation of K_{pvpv} and K_{pcpv} is depicted in Fig. 15(b). Far from the interaction point, when K_{pvpv} and K_{pcpv} were tuned at 0.31, the more damped situation was observed. The modal interaction was identified at the setting of K_{pvpv} and K_{pcpv} of 0.35, indicated by

the more oscillatory condition. Around an interaction point, small perturbation or variation of system parameter result in significant deviation of the engaged modes. One of the interacting modes departed remarkable toward the right half-open plane, resulting in deterioration of the system stability. Severe deterioration of the system dynamic response was identified. More oscillatory condition after interaction event due to a significant decrease of damping ratio was reported.

4. Conclusions

A detailed small-signal model of a hybrid MG considering dynamics of power electronics devices and its controllers was presented in this paper. Low and high-frequency critical modes corresponding to DGs output power and converter state variables
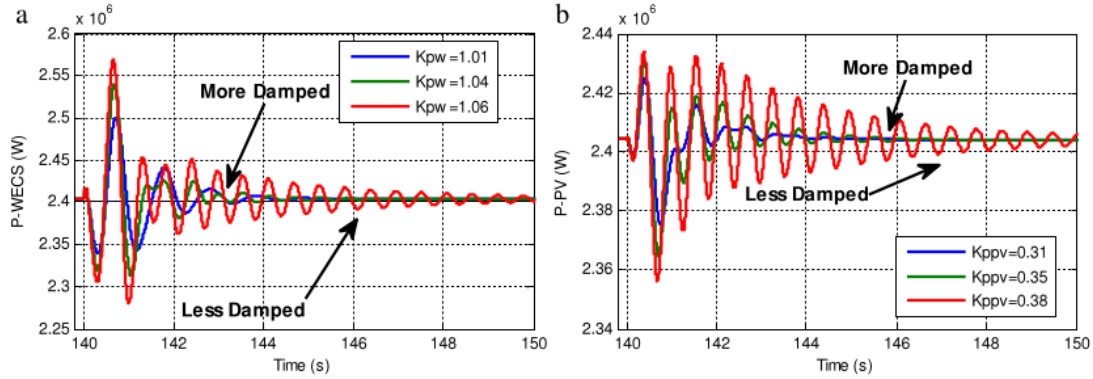
Fig. 15. (a) WECS and (b) PV active power influenced by modal interaction.

respectively, were significantly influenced by variation of gain controllers. Since the different architecture of DG units provides distinct small-signal stability features, evaluation of MG dynamic responses in many power-sharing strategies were investigated. The eigenvalues analysis and time domain simulation suggested that at higher contribution of PV and BDG based DG units, an enhanced system dynamic response was monitored. Moreover, the modal interaction potentially happen due to the proximity of the low-frequency critical modes. It could be a concern since it may cause resonance phenomenon which results in more oscillatory condition and lead to system instability. Obtained result regarding the comprehensive analysis of small-signal stability in autonomous operation of MG contributes to the design consideration and stability margin prediction of hybrid MG system.

The modal analysis is sufficient to investigate the oscillatory stability in hybrid MG under small variations of gain controllers. However, the presented method is not suitable for observing the dynamic behaviour of the MG system when it was subjected to unbalanced situations. The time domain simulation and Prony analysis methods are required for investigating the small signal stability performance of MG under unbalance situations. Moreover, the uncertain condition of RES and load have to be considered in investigating the MG stability. In future works, the effect of imbalance and uncertainties circumstances will be investigated to provide more practical and realistic scenario of MG operations.

Appendix

Parameter	Symbol	Value
Rated Voltage	V_{base}	690 V
Parasitic resistance of DC/DC inductor	R_b	1 mΩ
DC/DC inductor	L_b	2 mH
Parasitic resistance of DC/DC capacitor	R_{cb}	1 mΩ
DC/DC capacitor	C_b	1000 μF
AC input side Inductance of AC/DC	L_{sw}	1 mH
AC input side capacitor of AC/DC	C_{inw}	1000 μF
AC Side Resistance of AC/DC converter	R_{sdcw}	10 mΩ
DC Side Capacitor of DC/AC converter	C_{coutw}	1000 μF
DC Side Inductance of DC/AC inverter	L_{sdcw}	6.43 mH
DC Link inductance	L_{link}	0.01 mH
DC Link resistance	R_{link}	1 mΩ
DC Link Capacitance	C_d	6500 μF
Low Pass Filter Inductance	L_f	1 mH
Low Pass Filter Capacitance	C_f	100 μF
Low Pass Filter Resistance	R_f	1 mΩ
Coupling Inductance	L_c	0.1 mH
Coupling Resistance	R_c	1 mΩ

System parameters

Parameter	Symbol	Value
Load Resistance	R_{lo}	0.95 Ω
Load Inductance	L_{lo}	10 mH
Line Resistance (bus 1,2 and 3)	R_{lj}	10 mΩ
Line Inductance (bus 1,2 and 3)	L_{lj}	1 mH

References

[1] D. Gautam, V. Vittal, T. harbour, Impact of increased penetration of DFIG-based wind turbine generators on transient and small signal stability of power systems, IEEE Trans. Power Syst. 24 (3) (2009) 1426–1434.

[2] H. Liu, et al., Impact of high penetration of solar photovoltaic generation on power system small signal stability, in: Power System Technology (POWERCON), IEEE, Hangzhou, 2010, pp. 1–7.

[3] W. Zhou, et al., Current status of research on optimum sizing of stand-alone hybrid solar–wind power generation systems, Appl. Energy 87 (2010) 380–389.

[4] Z. Shuai, et al., Microgrid stability: Classification and a review, Renew. Sustain. Energy Rev. 58 (2016) 167–179.

[5] R. Majumder, Some aspects of stability in microgrids, IEEE Trans. Power Syst. 28 (3) (2013) 3243–3252.

[6] X. Tang, W. Deng, Z. Qi, Investigation of the dynamic stability of microgrid, IEEE Trans. Power Syst. 29 (2) (2014) 698–706.

[7] I.-P.T.f.o.M. Control, Trends in microgrid control, IEEE Trans. Smart Grid 5 (4) (2014) 1905–1919.

[8] M. Hamzeh, et al., Power oscillations damping in DC microgrids, IEEE Trans. Energy Convers. 31 (3) (2016) 970–980.

[9] N. Rashidirad, et al., A simplified equivalent model for the analysis of low-frequency stability of multi-bus DC microgrids, IEEE Trans. Smart Grid (2017).

[10] V. Bakic, et al., Dynamical simulation of PV/wind hybrid energy conversion system, Energy 45 (2012) 324–328.

[11] W. Deng, X. Tang, Z. Qi, Research on dynamic stability of hybrid wind/PV system based on micro-grid, in: Electrical Machines and System ICEMS, International Conference on, IEEE, Wuhan, 2008, pp. 2627–2632.

[12] N. Nimpitiwan, S. Kaitwanidvilai, Static output feedback robust loop shaping control for grid conncected inverter using genetic algorithms, Int. J. Innov. Comput. Inf. Control 8 (2012) 6081–6093.

[13] N. Kroutikova, C.A. Hernandez-Aramburo, T.C. Green, State-space model of grid-connected inverters under current control mode, IET Electr. Power Appl. 1 (3) (2007) 329–338.

[14] F. Katerei, M.R. Iravani, P.W. Lehn, Small-signal dynamic model of a micro-grid including conventional and electronically interfaced distributed resources, IET Gen. Transm. Distrib. 1 (3) (2007) 369–378.

[15] A. Krismanto, N. Mithulananthan, K.Y. Lee, Comprehensive modelling and small signal stability analysis of res-based microgrid, in: 9th IFAC Symposium on Control of Power and Energy Systems, CPES, Elsevier, New Delhi, India, 2015, pp. 282–287.

[16] J. Rocaber, et al., Control of power converters in AC microgrids, IEEE Trans. Power Electron. 27 (11) (2012) 4734–4749.

[17] N. Pogaku, M. Prodanovic, T.C. Green, Modeling, analysis and testing of autonomous operation of an inverter-based microgrid, IEEE Trans. Power Electron. 22 (2) (2007) 613–625.

[18] C.E. Ugalde-Loo, J.B. Ekanayake, N. Jenkins, State-space modeling of wind turbine generators for power system studies, IEEE Trans. Ind. Appl. 48 (2013) 223–232.

[19] P.C. Krause, O. Wasynczuk, S.D. Sudhoff, Analysis of Electric Machinery and Drive System, second ed., Wiley-Interscience, 2002.

[20] R.D. Middlebrook, S. Cuk, A general unified approach to modelling switching-converter power stages, in: Power Electronics Specialists Conference, Cleveland, 1976.

[21] R.W. Erickson, D. Maksimovic, Fundamental of Power Electronics, second ed., Kluwer Academic Publisher, University of Colorado Boulder, Colorado, 2001.

[22] R. Wu, S.B. Dewan, G.R. Slemon, A PWM AC-to-DC converter with fixed switching frequency, IEEE Trans. Ind. Appl. 26 (5) (1990) 880–885.

[23] A. Kahrobaeian, I. Mohamed Yasser Abdel-Rady, Analysis and mitigation of low-frequency instabilities in autonomous medium-voltage converter-based microgrids with dynamic loads, IEEE Trans. Ind. Electron. 61 (4) (2014) 1643–1658.

[24] Q.-C, Z. Hong, A.Y. Zeng, Universal droop control of inverters with different types of output impedance, IEEE Access 4 (2016) 702–712.

[25] N.A. Rahim, J.E. Quaicoe, Small signal model and analysis of a mulitple feedback control scheme for three phase voltage source UPS inverter, in: Proceedings of Power Electronics Specialist Conference, Boveno, Italy, 1996.

[26] I. Munteanu, A.I. Bratcu, N.-A.C.E. Ceang, Optimal Control of Wind Energy System, Springer-Verlag London Limited, London, 2008.

[27] R. Wu, S.B. Dewan, G.R. Slemon, Analysis of an AC-to-DC voltage source converter using PWM with phase and amplitude control, IEEE Trans. Ind. Appl. 27 (2) (1991) 12.

[28] O. Anaya-Lara, et al., Wind Generation: Modelling and Control, John Wiley & Sons, Ltd., 2009.

[29] Bin Wu, et al., Power Conversion and Control of Wind Energy Systems, Wiley, 2011.

[30] C.E. Ugalde-Loo, J.B. Ekanayake, State-space modelling of variable-speed wind turbines: A systematic approach, in: Sustainable Energy Technologies (ICSET), IEEE, Kandy, Sri Lanka, 2010, pp. 1–6.

[31] N. Kroutikova, C.A. Hernandez-Aramburo, T.C. Green, State-space model of grid-connected inverters under current control mode, IET Electr. Power Appl. 1 (3) (2007) 329–338.

[32] E. Barklund, et al., Energy management in autonomous microgrid using stability-constrained droop control of inverters, IEEE Trans. Power Electron. 23 (5) (2008) 2346–2351.

[33] L. Rese, A.S. Costa, A.S.e. Silva, Small-signal modeling and analysis of micro-grids including network and vsi dynamics, in: Power Energy Society General Meeting, IEEE, San Diego, 2012.

[34] K.V. Vidyanandan, N. Senroy, Primary frequency regulation by deloaded wind turbines using variable droop, IEEE Trans. Power Syst. 28 (3) (2013) 837–846.

[35] K.R. Padiyar, Analyis of Subsynchronous Resonance in Power System, Springer Science, New York, 1999.

[36] M.A. Abusara, S.M. Sharkh, J.M. Guerrero, Improved droop control strategy for grid-connected inverters, Sustain. Energy Grid Netw. 1 (2015) 10–19.

Small-Signal-Stability Enhancement using a Power-System Stabilizer based on the Cuckoo-Search Algorithm against Contingency N-1 in the Sulselrabar 150-kV System